


## Article

# A Phenomenological Study of Chromium Impurity Effects on Lattice Microstrains of SnO<sub>2</sub> Nanoparticles Prepared Using Sol–Gel Technique

Leili Motevalizadeh <sup>1,\*</sup> and Masoud Tahani <sup>2,3,\*</sup> <sup>1</sup> Department of Physics, Mashhad Branch, Islamic Azad University, Mashhad 91871-47578, Iran<sup>2</sup> Department of Mechanical Engineering, Ferdowsi University of Mashhad, Mashhad 91779-48974, Iran<sup>3</sup> Institute of Fundamental Technological Research, Polish Academy of Sciences, Pawińskiego 5B, 02-106 Warsaw, Poland

\* Correspondence: lmotevali@mshdiau.ac.ir (L.M.); mtahani@um.ac.ir or mtahani@ippt.pan.pl (M.T.)

**Abstract:** In this study, the effect of chromium impurities on the crystal structure and lattice microstrains of tin oxide nanoparticles was investigated. Pure SnO<sub>2</sub> nanoparticles were synthesized and subjected to calcination at different temperatures. Additionally, various concentrations (5%, 8%, 10% and 15%) of Cr-doped SnO<sub>2</sub> nanoparticles were prepared using the sol–gel technique and subsequently calcined at 550 °C. Transmission electron microscopy (TEM) and X-ray diffraction (XRD) techniques were utilized to examine the structure and morphology of the doped nanoparticles. The XRD patterns of tin oxide nanoparticles with different percentages of chromium impurities showed a tetragonal structure without any additional phase. The TEM images of pure SnO<sub>2</sub> nanoparticles showed a uniform distribution of size and shape, with relatively smaller sizes compared to Cr-doped nanoparticles. To investigate the peak broadening of Cr-doped SnO<sub>2</sub> nanoparticles, the Halder–Wagner method and Williamson–Hall models were employed to examine the effects of crystallite sizes and lattice strain. The results showed that increasing the impurity has a dual effect on nanoparticle sizes. Increasing the chromium impurity up to 8% led to an increase in compressive stress caused by the substitution of Sn ions with Cr ions on the crystal structure of rutile, resulting in an increase in the magnitude of lattice strain. However, when the chromium impurity was increased up to 15%, interstitial doping was preferred over substitutional doping. The compressive stress was subsequently converted to tensile stress, requiring the system to spend some of its energy to overcome the compressive stress, with the remaining energy reflected in the form of tensile stress. Furthermore, Fourier transform infrared (FTIR) spectra were obtained for all of the samples, confirming the XRD analyses.

**Keywords:** Cr-doped SnO<sub>2</sub>; sol–gel; Williamson–Hall models; Halder–Wagner method; microstrains



**Citation:** Motevalizadeh, L.; Tahani, M. A Phenomenological Study of Chromium Impurity Effects on Lattice Microstrains of SnO<sub>2</sub> Nanoparticles Prepared Using Sol–Gel Technique. *Crystals* **2023**, *13*, 919. <https://doi.org/10.3390/cryst13060919>

Academic Editors: Fedlu Kedir Sabir, Osman Ahmed Zelekew, Bedasa Abdisa Gonfa, Lemma Teshome Tufa, Noto Susanto Gultom and Andebet Gedamu Tamirat

Received: 27 April 2023

Revised: 29 May 2023

Accepted: 5 June 2023

Published: 7 June 2023



**Copyright:** © 2023 by the authors. Licensee MDPI, Basel, Switzerland. This article is an open access article distributed under the terms and conditions of the Creative Commons Attribution (CC BY) license (<https://creativecommons.org/licenses/by/4.0/>).

## 1. Introduction

Stannic oxide (SnO<sub>2</sub>, tin oxide), as a transparent n-type semiconductor, has numerous applications in a variety of areas, such as transparent electrodes in flat panel displays [1], gas sensors [2], solar cells [3], photocatalysts [4], photodiodes [5], lithium-ion batteries [6], biosensors [7], etc.

The broad scope of practical applications of tin oxide nanostructures is due to the specific properties of this semiconductor. Tin oxide is a non-stoichiometric crystal, and its crystals have a tetragonal rutile structure with space group D<sub>14</sub> (P4<sub>2</sub>/mnm). SnO<sub>2</sub> has a wide bandgap with a value of approximately 3.6 eV at room temperature [8]. This compound has very good transparency within the range of the visible light spectrum. The nanoparticles of this compound have a high surface-to-volume ratio, which improves their relevant surface properties, such as photocatalytic activity and surface reactivity. In addition, the effects of various impurities on improving the properties of these nanoparticles

have been widely studied [9–11]. The most important effect of impurities in semiconducting nanostructures is increasing the carrier density. Tin oxide exhibits n-type conductivity due to the presence of intrinsic defects, such as oxygen vacancies and interstitial tin atoms, in its tetragonal lattice. Another mechanism that influences carrier density in SnO<sub>2</sub> is related to dopant impurities. Among the different studied impurities, the transition metals dopants, such as vanadium [9], manganese [10], cobalt [11], nickel [12] and iron [13], have beneficial effects on changing and improving the electrical, optical and catalytic properties. Numerous studies have been conducted recently to investigate the doping of SnO<sub>2</sub> with non-metal elements, such as F [14] and S [15], using first-principles calculations and DFT. For example, the doping of SnO<sub>2</sub> with B and S introduced additional defect energy levels in the forbidden bandgap, thereby enhancing crystal conductivity [16]. The physical properties of tin oxide, in addition to impurity, strongly depend on the morphology and size of the nanostructures, which are, in turn, affected by the synthesis method. For instance, to achieve high capacity when using SnO<sub>2</sub> nanoparticles in lithium-ion batteries, very fine tin oxide particles are required [17]. Extensive efforts have been devoted to the synthesis and characterization of tin dioxide nanoparticles, owing to the broad utilization of SnO<sub>2</sub> and various methods, such as co-precipitation [18], sol–gel [19], hydrothermal [20], chemical vapor deposition [21], carbothermal [22] and environmentally friendly methods [7]. Among the manufacturing methods, the sol–gel technique has received more attention because of its low-temperature process, easy composition control and cost-effectiveness. Sol–gel is a wet method that offers higher homogeneity and purity in nanoparticle production compared to other methods, as well as greater reactivity [19].

XRD is widely employed to characterize nanoparticles, providing insights into their crystalline structure, phase nature, lattice parameters and grain size. The size of crystallites and the presence of defects are the main causes of the broadening of XRD peaks. Therefore, peak broadening is utilized to determine the crystallite size and lattice strain. Lattice strain is caused by crystal flaws, grain boundaries, stacking sources, impurities and lattice dislocations, while crystallite size measures the size of coherently diffracting domains [23–25].

In this study, XRD patterns of chromium-doped SnO<sub>2</sub> nanoparticles synthesized via the sol–gel process with varying percentages of impurity, are analyzed. The Halder–Wagner (H–W) and Williamson–Hall (W–H) analysis models are used to estimate the mean crystallite size and microstrain of all samples. Finally, the results for crystallite sizes from these methods are compared with those of the Scherer method. TEM is employed to examine the morphology of Cr-doped nanoparticles, while FTIR spectroscopy was used to conduct additional analysis on the samples.

## 2. Materials and Methods

### 2.1. Synthesis of Tin Oxide Nanoparticles Using the Sol–Gel Technique

Before the synthesis of Cr-doped SnO<sub>2</sub> nanoparticles, pure SnO<sub>2</sub> particles were prepared at different calcination temperatures (350, 450 and 550 °C), to determine the optimized calcination temperature. The properties of pure nanoparticles were studied using XRD and FTIR techniques and their results are given in Section 3.1. The results showed that a more suitable temperature for calcination would be 550 °C.

SnO<sub>2</sub> nanoparticles were synthesized by adding 50 mL pure ethanol and 0.1 mol SnCl<sub>2</sub>·2H<sub>2</sub>O to 50 mL de-ionized water, followed by magnetic stirring at 40 °C. The resulting solution was further stirred for half an hour at 40 °C using a magnetic stirrer. While stirring, ethylene glycol (polymerization agent) and citric acid (complexing agent) in a 2:1 and 3:1 ratio, respectively, to SnCl<sub>2</sub>·2H<sub>2</sub>O, were gradually added to the solution and dissolved under continuous stirring until a clear solution was achieved.

The mixture was transferred to a balloon and subjected to reflux at 120 °C for 3 h to yield a homogeneous and complex solution. The resulting product (the refluxed solution) was aged at 80 °C for 20 h with indirect heating to obtain an adhesive gel and at 80 °C for 4 h with direct heating to obtain a fluffy gel. After drying at 150 °C for 12 h, resulting in a

completely dried gel, the dried product was pulverized into powder using a mortar. The final powder was then calcined at different calcination temperatures (350, 450 and 550 °C) for 1.5 h.

## 2.2. Synthesis of Cr-Doped SnO<sub>2</sub> Nanoparticles Using the Sol–Gel Technique

To synthesize the Cr-doped SnO<sub>2</sub> nanoparticles with various doping contents (5, 8, 10 and 15%), the same procedure was followed. In order to dope, a certain amount of CrCl<sub>3</sub>·6H<sub>2</sub>O was added to the precursor solution and stirred, and then all steps were repeated to produce the dried powder. Finally, the obtained powder was calcined at 550 °C for 1.5 h.

## 2.3. Characterization

The characterization of the samples' crystalline phase and structure was performed using XRD with Cu-K $\alpha$  radiation. Transmission electron microscopy was employed to observe the morphology of the particles. These analyses provide valuable insights into the structural and morphological features of the products, which are essential for understanding their properties and potential applications. The FTIR spectra of the samples pressed with KBr in the range of 400 to 4000 cm<sup>-1</sup> were recorded.

## 2.4. Quantitative Analysis of XRD Data

### 2.4.1. Scherrer Method

The two primary characteristics obtained from the broadening of the XRD pattern are crystallite size and lattice strain. The size of a coherently diffracting domain can be measured as the crystallite size, which is commonly determined using the Scherrer method. This method suggests that peak broadening is a consequence of the crystallite sizes, and the average nanocrystallite size can be calculated using Debye–Scherrer's formula [26]:

$$D = \frac{K\lambda}{\beta_{hkl} \cos \theta'} \quad (1)$$

where,  $D$  is the size of the crystallite,  $K$  is the shape factor constant (almost equal to one for spherical particles),  $\lambda$  is the wavelength of Cu-k $\alpha$  radiation and  $\beta_{hkl}$  is the FWHM (full width at half maximum) of the peak [26].

The Scherrer equation solely addresses the impact of crystallite size on the broadening of the XRD peak and disregards the influence of lattice strain. To enhance the accuracy of crystallite size determination, both factors should be simultaneously taken into consideration. Two distinct types of strain, namely homogeneous and non-homogeneous lattice strains, should be considered as they influence the broadening and position of the peak, respectively [27–29].

### 2.4.2. Williamson–Hall Method

According to the Williamson–Hall approach, the broadening observed in the diffraction line is a result of both crystallite size and strain. In order to assess the strain resulting from lattice deformation, three modified Williamson–Hall (W–H) models have been proposed, which consider the uniformity or non-uniformity of the strain. The Williamson–Hall models consist of the uniform deformation model, the uniform stress deformation model and the uniform density energy deformation model known as UDM, USDM and UDEDM, respectively [27–29].

The UDM assumes the crystal to be isotropic and in this model, the broadening resulting from size ( $\beta_D$ ) and the broadening resulting from strain ( $\beta_S$ ) are assumed to be independent, and can be expressed as [26]:

$$\beta_{hkl} = \beta_D + \beta_S = \frac{K\lambda}{D \cos \theta} + 4\epsilon \tan \theta, \quad (2)$$

where,  $\varepsilon$  is the lattice strain. The above equation can be rewritten as follows [27]:

$$\beta_{hkl} \cos \theta = \frac{K\lambda}{D} + 4\varepsilon \sin \theta. \quad (3)$$

In USDM, the stress resulting from lattice deformation is assumed to be uniform in all directions of crystallography and the lattice strain is small. Consequently, the relation between stress ( $\sigma$ ) and strain ( $\varepsilon$ ) is linear and expressed by the equation  $\sigma = Y_{hkl} \varepsilon$ , where,  $Y_{hkl}$  is the proportionality constant and is called Young's modulus. Thus, Equation (3) is stated as follows [26]:

$$\beta_{hkl} \cos \theta = \frac{K\lambda}{D} + 4 \frac{\sigma}{Y_{hkl}} \sin \theta. \quad (4)$$

The directional dependent Young's modulus of SnO<sub>2</sub> nanoparticles which is related to elastic compliances and stiffness constants was calculated to be 118 GPa [25].

The UDEDM does not assume isotropy and homogeneity. Furthermore, when taking into account the strain energy density, the proportionality constants related to the stress–strain relation are no longer independent. The strain energy density ( $u$ ), the energy per unit volume for an elastic system obeying Hooke's law, can be calculated using the following equation:

$$u = \frac{1}{2} \sigma \varepsilon = \frac{1}{2} \varepsilon^2 Y_{hkl}. \quad (5)$$

The substitution of  $\varepsilon$  from Equation (5) into Equation (4) yields the Williamson–Hall equation in the following form [29]:

$$\beta_{hkl} \cos \theta = \frac{K\lambda}{D} + 4 \sin \theta \left( \frac{2u}{Y_{hkl}} \right)^{1/2}. \quad (6)$$

#### 2.4.3. Halder–Wagner Method

The Halder–Wagner method employs the Lorentzian and Gaussian functions to describe the crystallite size and strain profiles, respectively. The approach assumes that the broadening of the peak takes the form of a symmetric Voigt distribution, which arises from the convolution of Lorentzian and Gaussian functions [28]. The Halder–Wagner method provided an approximation for the integral breath of the Voigt function as follows [28]:

$$\beta_{hkl}^2 = \beta_L \beta_{hkl} + \beta_G^2, \quad (7)$$

where,  $\beta_L$  represents the Lorentzian component and  $\beta_G$  is the Gaussian component. The size of the crystallites and lattice strain are described in this model by [28],

$$\left( \frac{\beta_{hkl}^*}{d_{hkl}^*} \right)^2 = \frac{1}{D} \left( \frac{\beta_{hkl}^*}{d_{hkl}^{*2}} \right) + \left( \frac{\varepsilon}{2} \right)^2, \quad (8)$$

in which,

$$\beta_{hkl}^* = \beta_{hkl} \cos \theta / \lambda, \quad d_{hkl}^* = 2d_{hkl} \cos \theta / \lambda. \quad (9)$$

### 3. Results and Discussion

#### 3.1. Characterization of Pure SnO<sub>2</sub> Nanoparticles

Tin oxide nanoparticles were synthesized and subjected to calcination at various temperatures of 350, 450 and 550 °C. Table 1 presents the weights of the samples, measured both before and after the calcination process. From this table, the highest relative mass reduction is observed at the calcination temperature of 550 °C. Due to the higher relative reduction in mass at this specific temperature, it can be concluded that the majority of organic additives have been effectively eliminated from the material.

**Table 1.** The results of weighing SnO<sub>2</sub> powders before and after calcination at different temperatures for 1.5 h. The initial mass before heating was 4 g.

Calcination Temperature (°C)	Mass after Heating (g)	Relative Mass Reduction (%)
350	3.11	22.25
450	2.83	29.25
550	2.57	35.75

The X-ray diffraction pattern analysis of tin oxide nanoparticles at different calcination temperatures of 350, 450 and 550 °C, depicted in Figure 1, shows that all samples are single phase without any additional phase. The XRD patterns show that as the calcination temperature increases, the peaks become sharper which is related to an increase in the crystallite size of nanoparticles, enhancing the crystalline order and reducing lattice strain. The mean crystallite size for the samples prepared at different calcination temperatures of 350, 450 and 550 °C, were measured as 21.48, 24.11 and 26.59 nm, respectively.

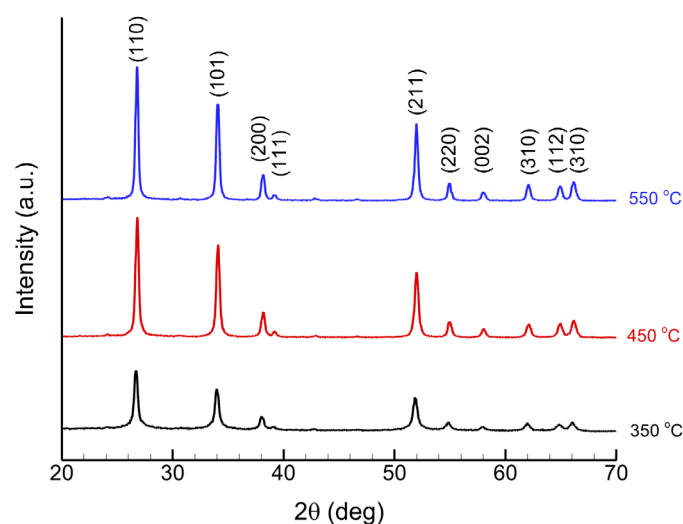


**Figure 1.** The X-ray diffraction patterns analysis of tin oxide nanoparticles at different calcination temperatures of 350, 450 and 550 °C.

Figure 2 displays the FTIR spectra of SnO<sub>2</sub> nanoparticles synthesized at different calcination temperatures. This figure shows that the peaks observed around 3400 and 1630 cm<sup>-1</sup> are attributed to the stretching vibrations of water molecules and hydroxide groups adsorbed on the surface of SnO<sub>2</sub> nanoparticles. With an increase in the temperature of calcination, these peaks decrease. The weak peaks around 2400 cm<sup>-1</sup> correspond to the stretching vibrations of CO<sub>2</sub>, and the peak at 1097 cm<sup>-1</sup> indicates the bending vibrations of C–O, while the peak at 1400 cm<sup>-1</sup> corresponds to both the bending and stretching vibrations of C–H. These suggest that some organic groups have been adsorbed on the surface of the powders. As observed in Figure 2, an increase in temperature leads to a decrease in these peaks which indicates the disappearance of organic materials from the samples. Two prominent absorption peaks at 623 and 470 cm<sup>-1</sup> correspond to the stretching modes of Sn=O and Sn–O, respectively, confirming the presence of crystalline SnO<sub>2</sub> [30]. Analysis of these results shows that preparing SnO<sub>2</sub> nanoparticles with calcination at 550 °C leads to an increase in the crystallite size of SnO<sub>2</sub> particles and the removal of organic additives.

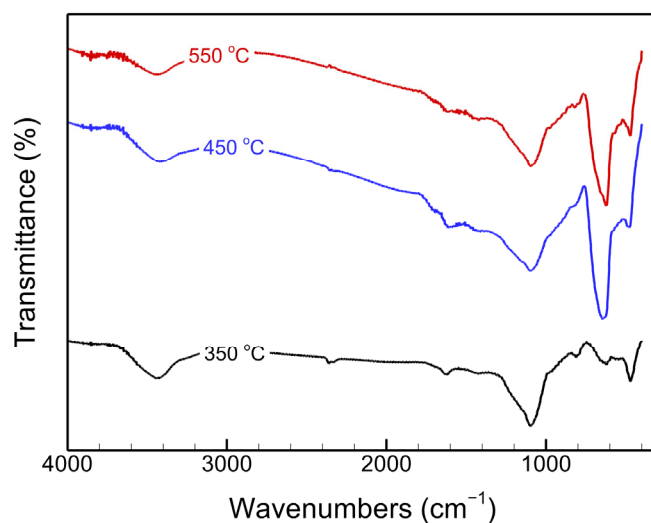


**Figure 2.** The FTIR spectra of SnO<sub>2</sub> nanoparticles calcined at different temperatures.

### 3.2. Characterization of Cr-Doped SnO<sub>2</sub> Nanoparticles

#### 3.2.1. The XRD Analysis

The XRD patterns of the samples with different Cr contents are illustrated in Figure 3. The diffraction peaks can be easily assigned to the tetragonal rutile configuration of SnO<sub>2</sub>. The absence of additional diffraction peaks signifies that the SnO<sub>2</sub> nanoparticles are solely composed of crystalline material. The sharp and narrow intensity of the peaks confirms that the sample possesses a high quality, excellent crystalline structure and small grain size.

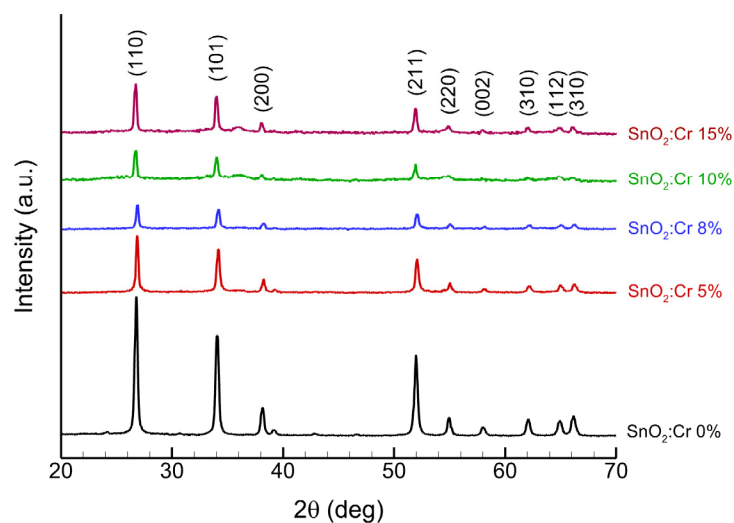


**Figure 3.** XRD patterns of Cr-doped SnO<sub>2</sub> nanoparticles with different Cr concentrations.

#### 3.2.2. Determination of Crystallite Size and Microstrain

To find the size of the crystallites and the strain in the samples using the methods described earlier, only the three prominent peaks of the (110), (101) and (211) planes evident in the XRD patterns, were taken into consideration.

In accordance with Equation (1) and Figure 4, for each sample, a line was plotted through the origin with  $\cos\theta$  on the  $y$ -axis and  $1/\beta$  on the  $x$ -axis. The Scherrer method was then employed to calculate the mean crystallite size. The results of this analysis are presented in Table 2.

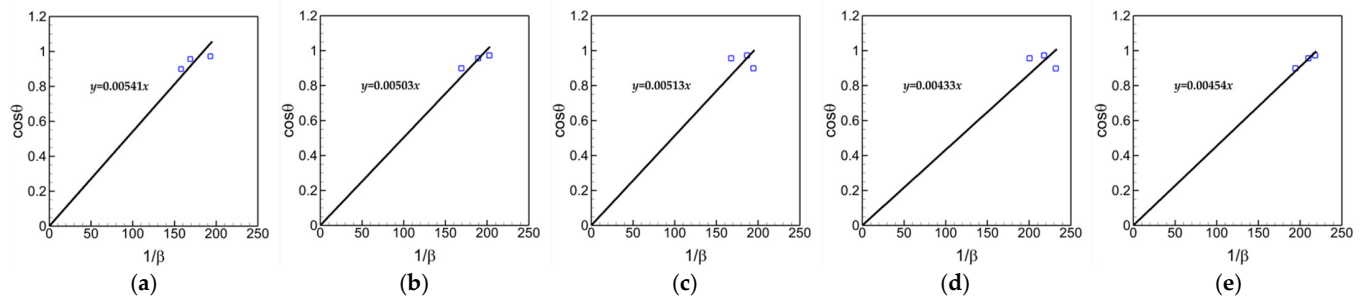


**Figure 4.** The fitted line using the Scherrer method for Cr-doped SnO<sub>2</sub> nanoparticles with (a) 0%, (b) 5%, (c) 8%, (d) 10% and (e) 15% Cr concentrations.

**Table 2.** Geometric parameters of chromium-doped tin oxide nanoparticles at various Cr concentrations.

Compound	Scherrer <i>D</i> (nm)	Williamson–Hall Method									Halder–Wagner Method	
		UDM		USDM			UEDM				<i>D</i> (nm)	$\epsilon \times 10^{-3}$
		<i>D</i> (nm)	$\epsilon \times 10^{-3}$	<i>D</i> (nm)	$\epsilon \times 10^{-3}$	$\sigma$ (MPa)	<i>D</i> (nm)	$\epsilon \times 10^{-3}$	$\sigma$ (MPa)	<i>u</i> (kJ·m <sup>3</sup> )		
SnO <sub>2</sub> :Cr 0%	26.75	31.37	0.66	31.37	0.73	85.90	31.37	0.66	78.06	25.76	32.20	6.0
SnO <sub>2</sub> :Cr 5%	28.85	33.65	0.59	33.69	0.59	69.47	33.69	0.59	69.50	20.45	69.33	4.9
SnO <sub>2</sub> :Cr 8%	28.22	22.78	−0.92	22.78	−0.92	−108.2	22.78	−0.92	−108.56	49.57	28.25	−2.8
SnO <sub>2</sub> :Cr 10%	33.68	26.45	−0.86	26.45	−0.86	−101.8	26.45	−0.86	−101.79	43.89	32.92	−2.8
SnO <sub>2</sub> :Cr 15%	31.88	33.59	0.19	33.59	0.19	21.88	33.59	0.19	21.95	2.03	35.04	2.8

The UDM data plot for the SnO<sub>2</sub> nanoparticles is shown in Figure 5, with  $4\sin\theta$  on the *x*-axis and  $\beta_{hkl} \cos\theta$  on the *y*-axis. Using Equation (3), the *y*-intercept and slope of the linear fit of the data in this figure were used to estimate the crystallite size, *D*, and microstrain,  $\epsilon$ , respectively. Furthermore, Figure 6 shows the USDM plots, where  $4\sin\theta/Y_{hkl}$  is plotted on the *x*-axis and  $\beta_{hkl} \cos\theta$  is plotted on the *y*-axis, and based on Equation (4), the crystallite size and microstrain values were determined. The plots drawn based on UEDM are also presented in Figure 7. The value of *u* (Equation (6)) was obtained from the slope and the crystallite size was obtained from the *y*-intercept of the linear fit of the plot between  $4\sin\theta(2/Y_{hkl})^{1/2}$  and  $\beta_{hkl} \cos\theta$ . Moreover, the plots generated using the Halder–Wagner method are shown in Figure 8. The values of  $\beta_{hkl}^*/d_{hkl}^{*2}$  and  $(\beta_{hkl}^*/d_{hkl}^*)^2$  were used to generate the plot; the crystallite size was determined from the slope of the linear fit, and the strain was calculated from the square root of the *y*-intercept. These results are summarized in Table 2.

Based on the results in Table 2, it can be observed that the lattice strains from the three methods (UDM, USDM and UEDM) based on the Williamson–Hall analysis do not differ significantly from each other. It is evident that the lattice strains calculated via different Williamson–Hall models are comparable with high accuracy. The lattice strain obtained using the Halder–Wagner method is found to be greater than that of the Williamson–Hall method. This significant difference could be attributed to the contribution of small angle X-ray scattering in the Halder–Wagner method. It seems that the lattice distortion has a considerable effect on the width of the peak located at smaller angles compared to the larger ones. Additionally, the average size of the crystallites obtained using the Halder–Wagner model is larger than that of the Williamson–Hall models [20].

It can be observed that initially, by adding the chromium content up to 5%, the value of strain decreases and subsequently, the crystallite size increases. With a further increase in impurities, the strain changes from tensile to compressive, resulting in a significant decrease in crystallite size. As the impurities increase up to 10%, the crystallites start to grow again due to the reduction in compressive strain and their size increases. Finally, with further increase in impurities, up to 15%, the strain changes back to tensile, and the crystallite size increases. This indicates that the lattice strains exhibited by the samples are not homogeneous and isotropic.

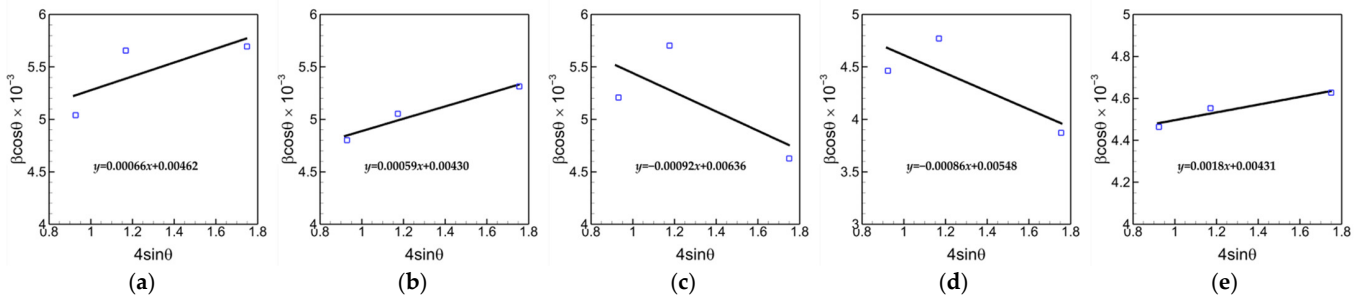


**Figure 5.** The fitted line using the UDM method for SnO<sub>2</sub> nanoparticles doped with (a) 0%, (b) 5%, (c) 8%, (d) 10% and (e) 15% Cr concentrations.

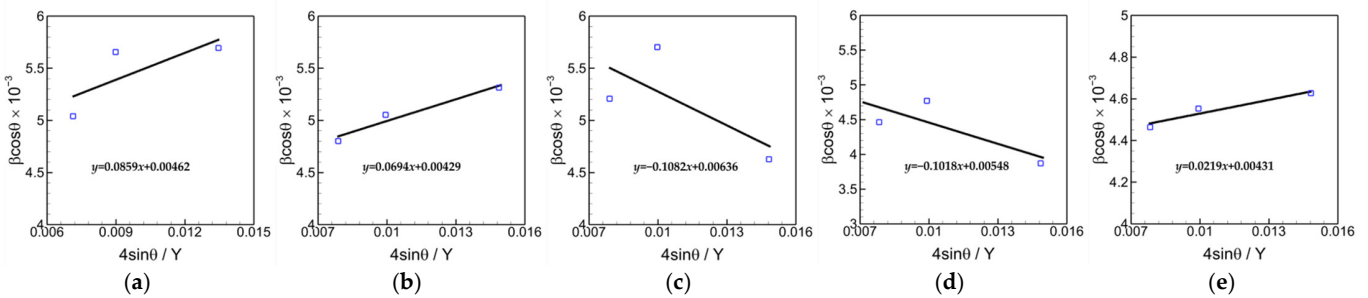


**Figure 6.** The fitted line using the USDM method for SnO<sub>2</sub> nanoparticles doped with (a) 0%, (b) 5%, (c) 8%, (d) 10% and (e) 15% Cr concentrations.

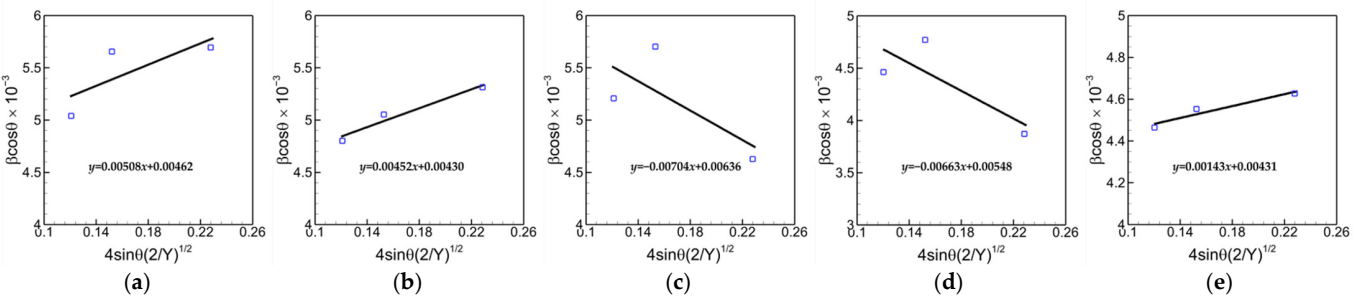


**Figure 7.** The fitted line using the UDEDM method for SnO<sub>2</sub> nanoparticles doped with (a) 0%, (b) 5%, (c) 8%, (d) 10% and (e) 15% Cr concentrations.

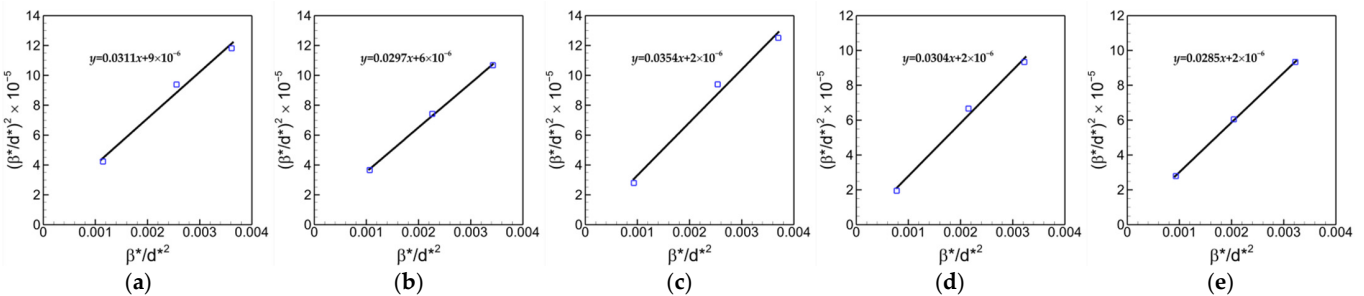


**Figure 8.** The fitted line using the Halder–Wagner method for Cr-doped SnO<sub>2</sub> nanoparticles with (a) 0%, (b) 5%, (c) 8%, (d) 10% and (e) 15% Cr concentrations.

This behavior can be explained by examining the mechanisms of Cr doping. The ionic radius of Cr<sup>3+</sup> (0.62 Å) is slightly smaller than that of Sn<sup>4+</sup> (0.69 Å), making them compatible. When Cr is doped up to 8%, it substitutes for Sn ion, as it has a smaller ionic radius, causing the lattice to contract. However, when the dopant is increased beyond 8%, it seems that the Cr ions, which are small enough to reside in the interstitial positions



of SnO<sub>2</sub> lattice, prefer to occupy the interstitial sites rather than the substitutional ones. Figure 9 schematically illustrates these two different types of sites in SnO<sub>2</sub> lattice.

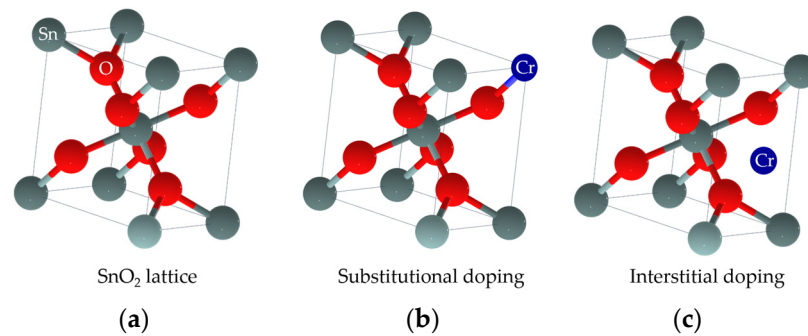


**Figure 9.** A visual representation depicting the atomic modification of the SnO<sub>2</sub> lattice by Cr doping, including both substitutional and interstitial sites. (a) SnO<sub>2</sub> lattice, (b) substitutional doping and (c) interstitial doping.

The results show that the initial substitution of chromium ions for tin ions reduces the strain and facilitates crystallite growth due to the smaller radius of chromium ions. However, with an increase in the concentration of chromium ions, up to 8%, the crystals begin to contract and the strains become compressive. When up to 10% of Cr concentration are added, it appears that rather than substituting tin ions, the chromium ions may occupy interstitial spaces, leading to a reduction in the compressive strain within the structure. When Cr ion is increased up to 15%, interstitial doping continues, the compressive strain vanishes and a tensile strain reappears.

### 3.2.3. Morphology Analysis

Figure 10 shows the TEM micrograph of the Cr-doped SnO<sub>2</sub> nanoparticles with different doping concentrations. The distribution of the prepared nanoparticles is in the order of crystallite sizes, ranging from 10 to 32 nm. Moreover, the nanoparticles present in the pure sample exhibit a uniform distribution of size and shape, with comparatively smaller sizes. However, with increasing Cr doping, the average particle size increases, which is consistent with the XRD analysis results. For low contents of Cr doping, the strain in the lattice decreases, allowing the particles to grow. At higher contents of Cr doping, up to 15%, the strain in the lattice increases. However, it seems that the occupation of interstitial sites by Cr ions compensates for the effect of lattice strain, thereby leading to the growth of nanoparticles. Therefore, regardless of how much impurity is induced in the SnO<sub>2</sub> lattice, the Cr-doped nanoparticles are larger than the pure ones.

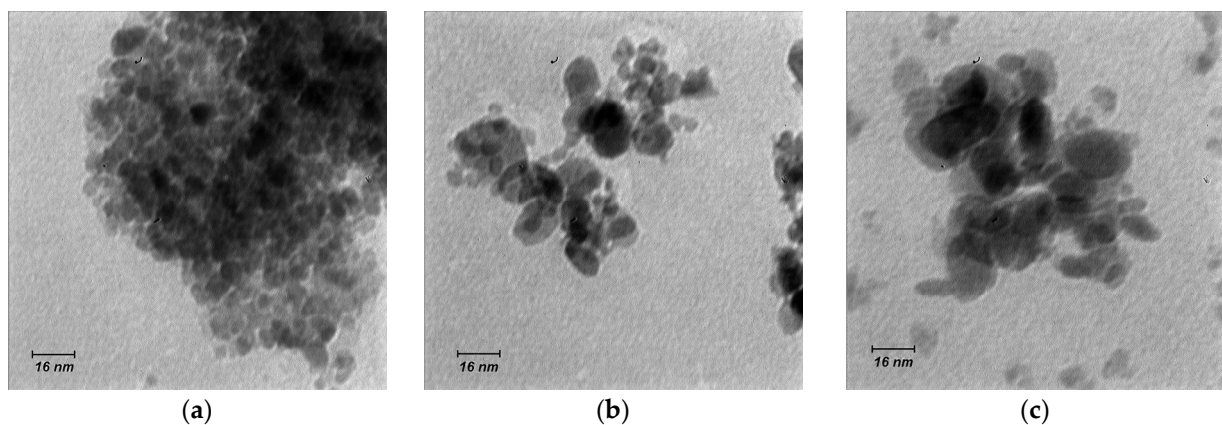


**Figure 10.** TEM of Cr-doped SnO<sub>2</sub> nanoparticles. (a) 0%, (b) 5% and (c) 15% Cr concentration.

### 3.2.4. FTIR Study

Figure 11 displays the FTIR spectra of SnO<sub>2</sub> nanoparticles doped with different Cr concentrations. The functional group region of the spectra, similar to Figure 2, indicates the low amounts of organic materials in the samples. The peaks below 1000 cm<sup>-1</sup>, referred to different modes of Sn–O and Cr–O. There are two large absorptive peaks near 623 and 470 cm<sup>-1</sup>, which correspond to the stretching modes of Sn=O and Sn–O, respectively [30]. Weak bands observed in the region 622–482 cm<sup>-1</sup> may be attributed to vibrations of νCr–O [31]. The spectra depicted in Figure 11 show that as the impurity content increases up to 5%, the two predominant peaks (623 and 470 cm<sup>-1</sup>) broaden and merge, accompanied by an increase in their intensity. This broadening and increase in peak intensity can be attributed to the entry of bands of νCr–O at 640 and 581 cm<sup>-1</sup>, as well as their merging with the stretching modes of Sn=O and Sn–O. When the impurity content is increased up to 8%, the intensity of the broad peak declines, and some tiny peaks emerge. As the intensity is associated with the molecular bonds, it can be said that adding Cr content up to 8% reduces the molecular bonds, leading to different peaks of Sn=O, Sn–O and emergence of νCr–O. This reduction occurs due to an increase in the substitution of Sn<sup>4+</sup> with a less charged Cr<sup>3+</sup> ion. As the Cr content is further increased, the two primary peaks begin to reappear. This suggests that adding more Cr content leads to interstitial residing and an increase in the molecular bonds of Sn–O and Sn=O. The FTIR spectra confirm that there are two different mechanisms in Cr doping which are governed by the amount of Cr concentration.

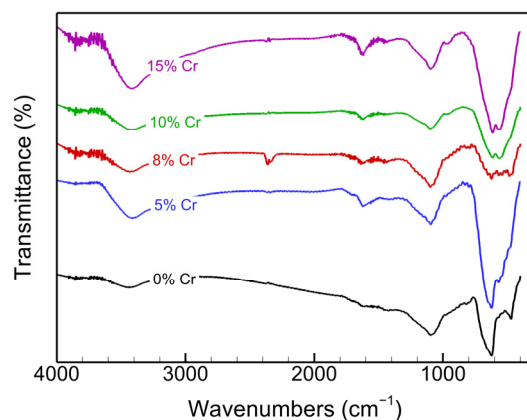


**Figure 11.** The FTIR spectra of SnO<sub>2</sub> nanoparticles doped with various Cr concentrations.

## 4. Conclusions

The effect of chromium impurities on the crystal structure and lattice microstrains of tin oxide nanoparticles was investigated using XRD analysis. Cr-doped SnO<sub>2</sub> nanoparticles were synthesized using the sol–gel method followed by calcination at 550 °C. The XRD peak broadening of all samples was analyzed using the Williamson–Hall models and the Halder–Wagner method to investigate the contributions of lattice strain and crystallite size. The XRD patterns showed the formation of pure SnO<sub>2</sub> with a rutile structure, and no impurity phases were detected. Our findings revealed that the impurity concentration has a dual effect on nanoparticle sizes. Specifically, an increase in chromium impurity up to 8% resulted in elevated compressive stress due to the substitution of Sn ions with Cr ions in the rutile crystal structure. However, when the impurities increased further, to 15%, Cr ions may prefer to occupy interstitial sites in SnO<sub>2</sub> lattice, resulting in a switch to tensile strain and an increase in the crystallite size. The morphological characterization using TEM indicated that the nanoparticles have diameters ranging from 10 to 32 nm. The FTIR spectra confirmed the dual behavior observed by doping SnO<sub>2</sub> nanoparticles, with a critical chromium concentration of 8%.

**Author Contributions:** Conceptualization, L.M. and M.T.; methodology, L.M.; software, M.T.; validation, L.M. and M.T.; formal analysis, M.T.; investigation, L.M.; resources, L.M.; data curation, M.T.; writing—original draft preparation, L.M.; writing—review and editing, L.M. and M.T.; visualization, L.M. All authors have read and agreed to the published version of the manuscript.

**Funding:** This research received no external funding.

**Data Availability Statement:** Data available on request due to restrictions, e.g., privacy.

**Conflicts of Interest:** The authors declare no conflict of interest.

## References

1. Dolatyari, M.; Jafari, A.; Rostami, A.; Klein, A. Transparent Display using a quasi-array of Si-SiO<sub>2</sub> Core-Shell Nanoparticles. *Sci. Rep.* **2019**, *9*, 2293. [\[CrossRef\]](#)
2. Kumar, R.; Mamta; Kumari, R.; Singh, V.N. SnO<sub>2</sub>-based NO<sub>2</sub> gas sensor with outstanding sensing performance at room temperature. *Micromachines* **2023**, *14*, 728. [\[CrossRef\]](#)
3. Lisnic, P.; Hrostea, L.; Leonti, L.; Girtan, M. Fluorine-doped SnO<sub>2</sub> thin films in solar cell applications. Morphological, optical and electrical properties. *Arch. Metall. Mater.* **2023**, *68*, 8.
4. Rangraz, Y.; Vahdat, S.M.; Khaksar, S. SnO<sub>2</sub> nanoparticles: A recyclable and heterogeneous catalyst for Pechmann condensation of coumarins and Knoevenagel condensation–Michael addition of biscoumarins. *Heliyon* **2023**, *9*, e15135. [\[CrossRef\]](#)
5. Ye, Q.; Zhang, X.; Yao, R.; Luo, D.; Liu, X.; Zou, W.; Guo, C.; Xu, Z.; Ning, H.; Peng, J. Research and progress of transparent, flexible tin oxide ultraviolet photodetector. *Crystals* **2021**, *11*, 1479. [\[CrossRef\]](#)
6. Park, J.-S.; Oh, Y.J.; Kim, J.H.; Kang, Y.C. Porous nanofibers comprised of hollow SnO<sub>2</sub> nanoplate building blocks for high-performance lithium ion battery anode. *Mater. Charact.* **2020**, *161*, 110099. [\[CrossRef\]](#)
7. Din, S.U.; Kiani, S.H.; Haq, S.; Ahmad, P.; Khandaker, M.U.; Faruque, M.R.I.; Idris, A.M.; Sayyed, M.I. Bio-synthesized tin oxide nanoparticles: Structural, optical, and biological studies. *Crystals* **2022**, *12*, 614. [\[CrossRef\]](#)
8. Drzymala, E.; Gruzal, G.; Depciuch, J.; Budziak, A.; Kowal, A.; Parlinska-Wojtan, M. Structural, chemical and optical properties of SnO<sub>2</sub> NPs obtained by three different synthesis routes. *J. Phys. Chem. Solids* **2017**, *107*, 100–107. [\[CrossRef\]](#)
9. Feng, C.; Li, X.; Wang, C.; Sun, Y.; Zheng, J.; Lu, G. Facile synthesis benzene sensor based on V<sub>2</sub>O<sub>5</sub>-doped SnO<sub>2</sub> nanofibers. *RSC Adv.* **2014**, *4*, 47549–47555. [\[CrossRef\]](#)
10. Ghodsi, F.E.; Mazloom, J. Optical, electrical and morphological properties of p-type Mn-doped SnO<sub>2</sub> nanostructured thin films prepared by sol–gel process. *Appl. Phys. A* **2012**, *108*, 693–700. [\[CrossRef\]](#)
11. Mazloom, J.; Ghodsi, F.E. Spectroscopic, microscopic, and electrical characterization of nanostructured SnO<sub>2</sub>:Co thin films prepared by sol–gel spin coating technique. *Mater. Res. Bull.* **2013**, *48*, 1468–1476. [\[CrossRef\]](#)
12. Chen, D.; Huang, S.; Huang, R.; Zhang, Q.; Le, T.-T.; Cheng, E.; Hu, Z.; Chen, Z. Convenient fabrication of Ni-doped SnO<sub>2</sub> quantum dots with improved photodegradation performance for Rhodamine B. *J. Alloys Compd.* **2019**, *788*, 929–935. [\[CrossRef\]](#)
13. Ali Baig, A.B.; Rathinam, V.; Ramya, V. Synthesis and Investigation of Fe doped SnO<sub>2</sub> Nanoparticles for Improved Photocatalytic Activity under Visible Light and Antibacterial performances. *Mater. Technol.* **2021**, *36*, 623–635. [\[CrossRef\]](#)
14. Ching-Prado, E.; Watson, A.; Miranda, H. Optical and electrical properties of fluorine doped tin oxide thin film. *J. Mater. Sci. Mater. Electron.* **2018**, *29*, 15299–15306. [\[CrossRef\]](#)
15. Li, W.; Ding, C.; Li, J.; Ren, Q.; Bai, G.; Xu, J. Sensing mechanism of Sb, S doped SnO<sub>2</sub> (1 1 0) surface for CO. *Appl. Surf. Sci.* **2020**, *502*, 144140. [\[CrossRef\]](#)
16. Yu, J.; Wang, Y.; Huang, Y.; Wang, X.; Guo, J.; Yang, J.; Zhao, H. Structural and electronic properties of SnO<sub>2</sub> doped with non-metal elements. *Beilstein J. Nanotechnol.* **2020**, *11*, 1321–1328. [\[CrossRef\]](#)
17. Bose, A.C.; Kalpana, D.; Thangadurai, P.; Ramasamy, S. Synthesis and characterization of nanocrystalline SnO<sub>2</sub> and fabrication of lithium cell using nano-SnO<sub>2</sub>. *J. Power Sources* **2002**, *107*, 138–141. [\[CrossRef\]](#)
18. Divya, J.; Pramothkumar, A.; Joshua Gnanamuthu, S.; Bernice Victoria, D.C.; Jobe Prabakar, P.C. Structural, optical, electrical and magnetic properties of Cu and Ni doped SnO<sub>2</sub> nanoparticles prepared via Co-precipitation approach. *Physica B* **2020**, *588*, 412169. [\[CrossRef\]](#)
19. Soo, M.T.; Kawamura, G.; Muto, H.; Matsuda, A.; Lockman, Z.; Cheong, K.Y. Design of hierarchically meso–macroporous tetragonal ZrO<sub>2</sub> thin films with tunable thickness by spin-coating via sol–gel template route. *Microporous Mesoporous Mater.* **2013**, *167*, 198–206. [\[CrossRef\]](#)
20. Motevalizadeh, L.; Heidary, Z.; Abrishami, M.E. Facile template-free hydrothermal synthesis and microstrain measurement of ZnO nanorods. *Bull. Mater. Sci.* **2014**, *37*, 397–405. [\[CrossRef\]](#)
21. Vallejos, S.; Selina, S.; Annanouch, F.E.; Gràcia, I.; Llobet, E.; Blackman, C. Aerosol assisted chemical vapour deposition of gas sensitive SnO<sub>2</sub> and Au-functionalised SnO<sub>2</sub> nanorods via a non-catalysed vapour solid (VS) mechanism. *Sci. Rep.* **2016**, *6*, 28464. [\[CrossRef\]](#)
22. Xie, H.; Yin, X.; Chen, P.; Liu, J.; Yang, C.; Que, W.; Wang, G. Solvothermal synthesis of highly crystalline SnO<sub>2</sub> nanoparticles for flexible perovskite solar cells application. *Mater. Lett.* **2019**, *234*, 311–314. [\[CrossRef\]](#)

23. Mustapha, S.; Ndamitso, M.M.; Abdulkareem, A.S.; Tijani, J.O.; Shuaib, D.T.; Mohammed, A.K.; Sumaila, A. Comparative study of crystallite size using Williamson-Hall and Debye-Scherrer plots for ZnO nanoparticles. *Adv. Nat. Sci. Nanosci. Nanotechnol.* **2019**, *10*, 045013. [[CrossRef](#)]
24. Tan, W.K.; Muto, H.; Kawamura, G.; Lockman, Z.; Matsuda, A. Nanomaterial fabrication through the modification of sol-gel derived coatings. *Nanomaterials* **2021**, *11*, 181. [[CrossRef](#)]
25. Muhammed Shafi, P.; Chandra Bose, A. Impact of crystalline defects and size on X-ray line broadening: A phenomenological approach for tetragonal SnO<sub>2</sub> nanocrystals. *AIP Adv.* **2015**, *5*, 057137. [[CrossRef](#)]
26. Mote, V.D.; Purushotham, Y.; Dole, B.N. Williamson-Hall analysis in estimation of lattice strain in nanometer-sized ZnO particles. *J. Theor. Appl. Phys.* **2012**, *6*, 6. [[CrossRef](#)]
27. Bindu, P.; Thomas, S. Estimation of lattice strain in ZnO nanoparticles: X-ray peak profile analysis. *J. Theor. Appl. Phys.* **2014**, *8*, 123–134. [[CrossRef](#)]
28. Al-Shomar, S.M.; Akl, A.A.; Mansour, D.; Hedhili, F.; Aslam, A.; Shaaban, E.R.; Mahmoud, S.A. Influence of Mo<sup>+2</sup> ion concentration on crystallization, microstructure, crystal imperfection and morphology of WO<sub>3</sub> sprayed thin films. *Mater. Res. Express* **2022**, *9*, 096404. [[CrossRef](#)]
29. Khorsand Zak, A.; Abd Majid, W.H.; Abrishami, M.E.; Yousefi, R. X-ray analysis of ZnO nanoparticles by Williamson-Hall and size-strain plot methods. *Solid State Sci.* **2011**, *13*, 251–256. [[CrossRef](#)]
30. Abruzzi, R.C.; Dedavid, B.A.; Pires, M.J.R. Characterization of tin dioxide nanoparticles synthesized by oxidation. *Cerâmica* **2015**, *61*, 328–333. [[CrossRef](#)]
31. Bumajdad, A.; Al-Ghareeb, S.; Madkour, M.; Sagheer, F.A. Non-noble, efficient catalyst of unsupported  $\alpha$ -Cr<sub>2</sub>O<sub>3</sub> nanoparticles for low temperature CO Oxidation. *Sci. Rep.* **2017**, *7*, 14788. [[CrossRef](#)]

**Disclaimer/Publisher's Note:** The statements, opinions and data contained in all publications are solely those of the individual author(s) and contributor(s) and not of MDPI and/or the editor(s). MDPI and/or the editor(s) disclaim responsibility for any injury to people or property resulting from any ideas, methods, instructions or products referred to in the content.